APL Materials

Probing the structure of vanadium tetracyanoethylene using electron energy-loss spectroscopy

Cite as: APL Mater. **10**, 081102 (2022); https://doi.org/10.1063/5.0087997
Submitted: 11 February 2022 • Accepted: 04 July 2022 • Published Online: 02 August 2022

Amanda H. Trout, Seth W. Kurfman, Yueguang Shi, et al.

Probing the structure of vanadium tetracyanoethylene using electron energy-loss spectroscopy

Cite as: APL Mater. 10, 081102 (2022); doi: 10.1063/5.0087997
Submitted: 11 February 2022 • Accepted: 4 July 2022 •
Published Online: 2 August 2022

Amanda H. Trout,[1,2] Seth W. Kurfman,[3] Yueguang Shi,[4] Michael Chilcote,[3] Michael E. Flatté,[4,a)] Ezekiel Johnston-Halperin,[3,b)] and David W. McComb[1,2,c)]

AFFILIATIONS

[1] Center for Electron Microscopy and Analysis, Ohio State University, Columbus, Ohio 43212, USA
[2] Department of Materials Science and Engineering, Ohio State University, Columbus, Ohio 43210, USA
[3] Department of Physics, Ohio State University, Columbus, Ohio 43210, USA
[4] Department of Physics and Astronomy, University of Iowa, Iowa City, Iowa 52242, USA

[a)] michael-flatte@uiowa.edu
[b)] johnston-halperin.1@osu.edu
[c)] **Author to whom correspondence should be addressed:** mccomb.29@osu.edu

ABSTRACT

The molecule-based ferrimagnetic semiconductor vanadium tetracyanoethylene ($V[TCNE]_x$, $x \approx 2$) has garnered interest from the quantum information community due to its excellent coherent magnonic properties and ease of on-chip integration. Despite these attractive properties, a detailed understanding of the electronic structure and mechanism for long-range magnetic ordering have remained elusive due to a lack of detailed atomic and electronic structural information. Previous studies via x-ray absorption near edge spectroscopy and the extended x-ray absorption fine structure have led to various proposed structures, and in general, $V[TCNE]_x$ is believed to be a three-dimensional network of octahedrally coordinated V^{2+}, each bonded to six TCNE molecules. Here, we elucidate the electronic structure, structural ordering, and degradation pathways of $V[TCNE]_x$ films by correlating calculations of density functional theory (DFT) with scanning transmission electron microscopy and electron energy-loss spectroscopy (EELS) of $V[TCNE]_x$ films. Low-loss EELS measurements reveal a bandgap and an excited state structure that agree quantitatively with DFT modeling, including an energy splitting between apical and equatorial TCNE ligands within the structure, providing experimental results directly backed by theoretical descriptions of the electronic structure driving the robust magnetic ordering in these films. Core-loss EELS confirms the presence of octahedrally coordinated V^{+2} atoms. Upon oxidation, changes in the C1s-π^* peak indicate that C = C of TCNE is preferentially attacked. Furthermore, we identify a relaxation of the structural ordering as the films age. These results lay the foundation for a more comprehensive and fundamental understanding of magnetic ordering and dynamics in these classes of metal–ligand compounds.

I. INTRODUCTION

As the field of quantum information science progresses, so too does the desire for materials that are both compatible with existing technology frameworks and capable of effectively contributing to quantum-coherent operations.[1,2] Magnon-based hybrid quantum systems are specifically enticing for such application as their low-lying collective magnetic excitations, known as magnons (the quanta of spin waves), can coherently couple to a variety of quantized excitations, including photons, phonons, and localized spin transitions,[3,4] and also their microwave resonance frequencies are commensurate with those of quantum information processing. The traditional material choice for these low-loss magnonics applications is yttrium iron garnet ($Y_3Fe_5O_{12}$ aka YIG), which has been shown to be an attractive candidate material for magnonic/spintronic applications[5–7] and magnon-based quantum systems.[2,8] However,

the processing techniques required to produce high-quality low-loss YIG microstructures on-chip for these magnon-based hybrid quantum systems remain a substantial obstacle.[9] Solutions to these hurdles may still come to fruition for YIG or other low-loss ferrites; however, reliance on a single material class substantially limits the capabilities and applicability of these integrated systems.

To bypass these challenges, an alternative ferrimagnetic material has been proposed,[4] the organic-based coordination compound vanadium tetracyanoethylene ($V[TCNE]_x$). $V[TCNE]_x$ is a low-loss ($\alpha \sim 4 \times 10^{-5}$) ferrimagnetic semiconductor with a Curie temperature (T_c) > 600 K[5] that exhibits magnetic resonance quality factors $Q > 7000$ (at 6 GHz) and has rapidly gained attention as a material in magnon-based quantum systems.[4,10–12] $V[TCNE]_x$ can be easily deposited as high-quality thin films on a variety of bare or patterned substrates,[13] and modified electron-lithography techniques have demonstrated that the material can be patterned into microstructures with a negligible increase in its magnetic damping.[11,12] The patterning capability of this low-loss insulating ferrimagnet provides ample opportunity to integrate magnetic microstructures on-chip that extends its use in magnon-based devices.[14] Furthermore, low temperature ferromagnetic resonance (FMR) measurements reveal that $V[TCNE]_x$ retains its low-damping properties even at cryogenic temperatures, demonstrating its potential for use in low temperature quantum information science and engineering (QISE) applications.[12] Established measurements of optically detected FMR (ODFMR) in $V[TCNE]_x$ via diamond NV-centers, combined with its predicted ability to couple NV centers in diamond over micrometer lengthscales,[4] further bolster $V[TCNE]_x$ as a magnetic material for quantum information in solid-state systems.

Based on these exceptional properties, there has been growing interest in the use of molecular-based materials, including $V[TCNE]_x$ and its class of metal–ligand compounds, as alternatives in quantum systems as they provide significant advantages in their tunability and on-chip integration over more traditional inorganic materials and ferrites, such as YIG.[12,15–22] $V[TCNE]_x$ belongs to a broad class of $M[A]_x$ (M = metal and A = acceptor) organic-based magnetic materials[12,23–28] that remains relatively unexplored. A detailed and thorough understanding of $V[TCNE]_x$ will develop the foundation for a better understanding of other remarkable metal–ligand magnets and, thus, establish a clear path toward their applications in magnon-based QISE.

Despite the canonical role $V[TCNE]_x$ has held in the development and application of this class of material as a result of its excellent magnetic resonance properties, the understanding of its electronic and atomic structure is still largely phenomenological. $V[TCNE]_x$ films typically have high structural disorder or are amorphous, and the material is extremely air-sensitive when not encapsulated, making characterization challenging.[19–21,29–31] X-ray absorption fine structure (XAFS) studies have shed some light on the environment of vanadium, leading to the prediction of a 3D structure of V^{2+} in octahedral coordination with six surrounding TCNE molecules.[31–34] Previous *ab initio* calculations supported semiconducting behavior, an octahedral coordination of V^{2+}, and suggested that within the band structure, there were effective spin-splittings of ~2 eV for TCNE molecular orbitals and larger for the vanadium *d* states.[19] However, because x-ray diffraction (XRD) studies suggest that the material is amorphous, it is less clear which electronic properties from a crystalline calculation survive in the actual material.

In order to probe the structure of this highly disordered material, higher spatial resolution studies are needed. Electron energy-loss spectroscopy (EELS) performed in a scanning transmission electron microscope (STEM) is a powerful characterization technique that can be used to study various aspects of a material, including the composition, oxidation state, and bonding/coordination environment of atoms in the specimen, as well as the optoelectronic properties of the material. Here, we report the study of $V[TCNE]_x$ films grown by chemical vapor deposition (CVD) using STEM EELS. Low-loss EELS data backed by density functional theory (DFT) calculations provide insights into the electronic, magnetic, and spintronic properties of $V[TCNE]_x$. EELS spectra calculated directly from the *ab initio* structure based on the crystalline electronic structure match remarkably well with those measured, down to small details. Clear support is obtained for a revised schematic picture of the electronic structure, which distinguishes apical and equatorial TCNE molecular orbitals and vanadium *d* states. Furthermore, EELS data collected on multiple plan-view specimens indicate the high-quality CVD growth of $V[TCNE]_x$ and provide previously unknown information on the oxidation mechanism and an additional thermodynamic structural change as noted by the relaxation of the structure over time.

II. METHODOLOGY

A. CVD growth

$V[TCNE]_x$ films are deposited via ambient-condition chemical vapor deposition (CVD) in a custom CVD reactor inside an argon glovebox (O_2 < 1 ppm, H_2O < 1 ppm) in accordance with the literature.[21] Argon gas flows over TCNE and $V(CO)_6$ precursors that react to form a $V[TCNE]_x$ thin film on the substrates. The pressure inside the CVD reactor for all growths was 35 mmHg, and TCNE, $V(CO)_6$, and the substrates are held at 65, 10, and 50 °C, respectively. All substrates were cleaned with the solvent chain [acetone, methanol, isopropanol, and deionized (DI) water (x2)] and dried with N_2, followed by a 10 min UV/ozone clean in a UVOCS T10× 10/OES to remove any residual organic contaminants.

B. TEM sample preparation and transportation

For focused ion beam (FIB) foil samples, nominally, 400 nm thick $V[TCNE]_x$ films were deposited on commercially available 400 μm-thick p-doped Si substrates. These samples were, then, capped with 30 nm of Al deposited via thermal evaporation with a BOC Edwards Auto 500 deposition system housed inside an argon glovebox so that the $V[TCNE]_x$ films were not exposed to oxygen between the $V[TCNE]_x$ and Al deposition. The 30 nm cap served as an oxygen barrier for loading the samples into the FIB and was deposited in two 15 nm depositions to prevent $V[TCNE]_x$ films from overheating during the deposition. After capping with Al, samples are transferred under argon and exposed momentarily to air while loading into the FIB microscope. Cross-sectional FIB specimens were prepared using a FEI Helios NanoLab 600 DualBeam FIB/SEM. FIB foils were, then, loaded as quickly as possible into the microscope to avoid oxidation confirmed by the EELS spectra in Fig. S3.

For the plan-view samples, nominally, 100 nm thick V[TCNE]$_x$ films were deposited on 3 nm-thick Pt and Pd Substratek™ TEM grids purchased from Ted Pella. For each growth, 3 Pd and 3 Pt Substratek TEM grids were used, resulting in six potential TEM specimens, the best of which were loaded into a Gatan vacuum transfer holder inside the glovebox. This TEM sample holder allowed for transportation from the glovebox into the microscope without exposure to air.

In each growth, commercially available 430 μm-thick C-plane sapphire substrates were included as calibration samples for ferromagnetic resonance (FMR) characterization.

C. Magnetic characterization

Ferromagnetic resonance (FMR) measurements were performed in an x-band (9.8 GHz) Bruker Elexsys E500 CW electron paramagnetic resonance (EPR) spectrometer. The frequency of the microwave source is tuned to match the resonant frequency of the cavity before each scan to ensure optimal cavity tuning. All scans had a 0.03 G modulation field at 100 kHz modulation frequency and were performed at the lowest possible microwave power (0.2 μW) to prevent sample heating and non-linear effects distorting the FMR line shape. V[TCNE]$_x$ films deposited on sapphire were mounted on a custom Macor ceramic sample holder and loaded into sealed quartz EPR tubes for FMR measurements. Samples were rotated in-plane (IP) to out-of-plane (OOP) for FMR measurements in 10° increments.

D. STEM EELS

Electron energy-loss spectroscopy data were collected on a FEI image corrected Titan3 G2 60–300 kV S/TEM equipped with a Gatan Quantum spectrometer and a K2 direct electron detector. Dual EELS spectrum images were collected at an operating voltage of 300 kV using a monochromator. The data were collected at a convergence semi-angle of 5.54 mrad and a collection semi-angle of 10.71 mrad. The exposure times were 0.0001 s for the low-loss region and 0.3 or 5 s for the high-loss region.

Low-loss EELS data were collected at an operating voltage of 60 kV to avoid Cherenkov radiation. The 60 kV data were collected at a convergence semi-angle of 9.3 mrad and a collection semi-angle of 18.04 mrad. In order to observe low eV transitions, the zero-loss peak (ZLP) was shifted slightly off the detector by setting the drift tube to 3 eV, and the exposure time for these datasets was 0.3 s. Low-loss EELS processing included the removal of the zero-loss peak (ZLP) using the reflected tail method and deconvolution using the Fourier-log method. High-loss data processing included a background subtraction before each edge of interest and deconvolution using the Fourier ratio method.

E. DFT calculations

The pseudopotentials used are default options from the official projector augmented wave (PAW) potential set of the Vienna *ab initio* Simulation Package (VASP), with five valence electrons per vanadium, four per carbon, and five per nitrogen.[35,36] For the rest of the calculation, we used 400 eV for the energy cutoff and a Γ centered 5 × 5 × 3 k-mesh sampling. The plots in Fig. S3 show the detailed partial density of states for majority and minority spins, associated with the vanadium d electrons and the equatorial (planar) and apical carbon or nitrogen p orbitals. These partial densities of states suggest that there is an effective U of ~5 eV between majority and minority vanadium d levels and of ~2 eV between majority and minority p levels of carbon and nitrogen. They also suggest a ligand field splitting of 1 eV between the equatorial and apical TCNE molecule *p* states.

III. RESULTS AND DISCUSSION

Following the CVD growth of V[TCNE]$_x$ films as described in Sec. II, the magnetic properties were measured to determine the quality of the material. The ultra-narrow, single-peak FMR spectra throughout the angular measurements confirm that the V[TCNE]$_x$ films are of high-quality. The in-plane (IP) and out-of-plane (OOP) peak-to-peak (full width at half max, FWHM) linewidths are 0.54 Oe (0.94 Oe) and 0.69 Oe (1.14 Oe), respectively (Fig. 1, insets). These linewidths correspond to FMR quality factors $Q = \frac{H_R}{\Delta H} > 3000$ for all field orientations, where H_R is the FMR resonant field and ΔH is the FWHM linewidth. The angular FMR resonance positions for the thin film shown in Fig. 1 are fit to the following equation:[21,37,38]

$$\frac{\omega}{\gamma} = \sqrt{\left(H_R - 4\pi M_{eff}\cos^2(\theta)\right)\left(H_R - 4\pi M_{eff}\cos(2\theta)\right)}, \quad (1)$$

where ω is the resonance frequency, γ is the gyromagnetic ratio, H_R is the external field, M_{eff} is the effective magnetization of the V[TCNE]$_x$ film, and θ is the field angle with respect to the film normal. This equation assumes that the magnetization and external magnetic field are parallel, which is appropriate since $M_{eff} \ll H_R$; therefore, we do not need to consider separate angles for the external field and magnetization.[11] Fitting to this equation yields $4\pi M_{eff}$ = 99.5 G, which is consistent with the previous literature values.[11–14,21,39] We do not see any IP anisotropy in these films, consistent with the previous work.[11]

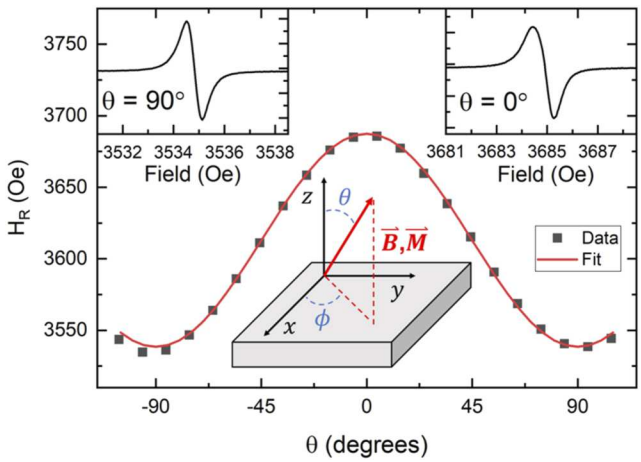

FIG. 1. Ferromagnetic resonance (FMR) position vs applied field angle $\theta(\phi = 0)$. Data are fit to the Kittel equation for a thin film with only shape anisotropy contributions, finding $4\pi M_{eff}$ = 99.5 G. The center diagram shows the defined coordinate system. Left inset: FMR linescan for in-plane magnetization (θ = 90°), showing single-peaked FMR in the V[TCNE]$_x$ film. Right inset: FMR linescan for out-of-plane magnetization (θ = 0°).

While V[TCNE]$_x$ has excellent low-loss magnetic properties, its electronic properties still leave much to explore and understand. Due to its sensitivity to air and high temperatures,[18,40] its electronic properties have predominately been measured via electric transport methods. Transport studies suggest that V[TCNE]$_x$ is a semiconductor with 0.5 eV bandgap and spin-polarized subbands; however, there are systematic limitations in these measurements, which reduce the precision and accuracy in extracting the bandgap.[41–43] Mott variable-range hopping (VRH) has been proposed in some studies, but more recent measurements suggest that this mechanism does not accurately describe electronic transport in V[TCNE]$_x$.[41–43] Thus, the mechanism for charge transport remains elusive. A more complete understanding of the electronic transitions in V[TCNE]$_x$ would provide a framework upon which to design future studies to investigate electronic transport, the optoelectronic properties, and the long-range magnetic ordering of V[TCNE]$_x$ films.

For example, the low-loss EELS spectrum, which contains energy-losses up to 50 eV, can be used to study the optoelectronic properties of a material. The single scattering distribution [$J^1(E)$] of the EELS spectrum is related to the complex dielectric function [$\varepsilon(E)$] by

$$J^1(E) = \frac{I_0 t}{\pi a_0 m_0 v^2} \mathrm{Im}\left[\frac{-1}{\varepsilon(E)}\right] \ln\left[1 + \left(\frac{\beta}{\theta_E}\right)^2\right], \quad (2)$$

where I_0 is the intensity of the zero loss peak (ZLP), t is the specimen thickness, a_0 is the Bohr radius, m_0 is the electron rest mass, v is the velocity of the primary electrons, β is the collection semi-angle, and θ_E is the characteristic scattering angle for specific energy-loss.[44] The raw EELS spectrum is a convolution of single and multiple scattering events; therefore, to extract $J^1(E)$, a deconvolution is performed in DigitalMicrograph (DM),[45] as described in Sec. II. The real [$\varepsilon_1(E)$] and imaginary [$\varepsilon_2(E)$] parts of the complex dielectric function can, then, be extracted from $J^1(E)$ by performing Kramers–Kronig (KK) analysis.[44–46]

Figure 2(a) shows low-loss data of a plan-view V[TCNE]$_x$ specimen that was collected at 60 kV to avoid Cherenkov radiation.[44,47]

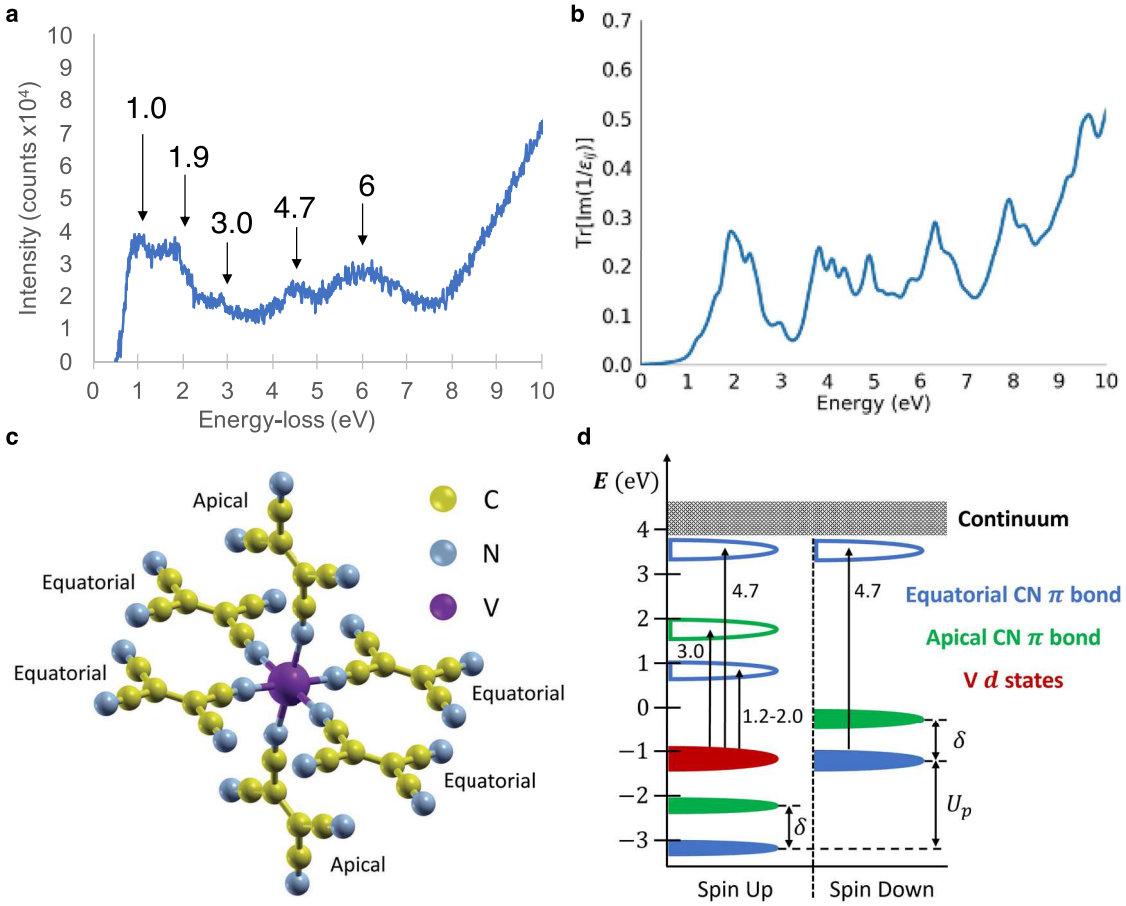

FIG. 2. (a) Low-loss EELS of a plan-view V[TCNE]$_x$ specimen collected at 60 kV after the removal of the ZLP. (b) Low-loss function calculated from the partial density of states using DFT. (c) Structure of V[TCNE]$_x$ used in DFT calculations. (d) Schematic display of the electronic transitions observed in low-loss EELS and supported by DFT calculations. δ represents the crystal field energy splitting equatorial and apical TCNE molecules, and U_p represents Hubbard U spin-splitting the p states.

The ZLP is the most intense peak in the EELS spectrum and is comprised of electrons that have passed through the specimen losing zero to a very little energy. The ZLP is needed to (i) calibrate the EELS spectrum and (ii) perform deconvolution and KK analysis. However, due to the intensity of the ZLP, it is difficult to observe low energy transitions without saturation. We, therefore, collected a low-loss spectrum with the ZLP partially shifted off the detector in order to increase exposure times (Fig. S1a). The right tail of the ZLP was, then, fit to an exponential function to remove the ZLP contribution from the low-loss spectrum (Fig. S1b). We compared this method to additional datasets in which KK analysis was performed in DM after the ZLP was removed using the reflected tail method, and the results do not differ (Fig. S1c).

After the removal of the ZLP, multiple single electron transitions can be observed in the low-loss EELS spectrum in Fig. 2(a). The onset of intensity provides a measure of the bandgap of the material, and here, we measure a bandgap of ~0.6 ± 0.18 eV. These measurements are consistent with previous bandgap EELS measurements collected at 60 kV from a FIB foil (Fig. S1c).

Ab initio density functional theory calculations provide further insights into the nature of the electronic transitions in Fig. 2(a). The electronic structure and dielectric function of $V[TCNE]_x$ was calculated using the Vienna *ab initio* Simulation Package (VASP) (version 5.4.4) with a plane wave basis, projector-augmented-wave pseudopotentials,[48–51] and a generalized gradient approximation of Perdew, Burke, and Ernzerhof (PBE).[52] The hybrid Heyd–Scuseria–Ernzerhof (HSE06) functional[53] with range separation parameter $\omega = 0.2$ incorporates an admixture of Hartree–Fock energies with PBE to improve the accuracy of the bandgap calculations. The structure is very similar to that obtained in Ref. 19 although the details of the electronic structure, including the bandgap and band ordering, appear to differ from those reported there. Detailed plots of the partial densities of states are shown in the supplementary material (Fig. S2). From this, we calculate the loss function averaged over all momentum transfers, $\mathrm{Tr}(1/\varepsilon)$, shown in Fig. 2(b). The general features show remarkable agreement with the experimentally measured low-loss data. It should be noted that while the energetic positions of the peaks align well, the peak intensities do not due to an assumption of an infinite periodic lattice in the DFT model. Thus, the matrix/symmetry elements likely differ between the calculation and experimental data as the DFT calculation is performed for a single crystal that is oriented; however, as-grown films are not single crystal and are randomly oriented.

A schematic band ordering from our calculations is shown in Fig. 2(d), which suggests an approximate effective U for the vanadium *d* states of ~5 eV and for the π orbitals of ~2 eV, along with a ligand field splitting between the equatorial and apical TCNE molecules of ~1 eV. The V–N bond lengths of the apical and equatorial TCNE molecules are very similar, preserving the octahedral point symmetry of the V ion; the apical/equatorial molecule distinction emerges because only two of the apical TCNE nitrogen molecules bond to vanadium, whereas all four in an equatorial TCNE molecule bond to vanadium. The result is a small (~1 eV) ligand field splitting for the C–N π bond. We note that while the local V-cyano coordination is similar for all the six TCNE bonded to central V, the apical TCNE molecules are not fully coordinated to adjacent V, e.g., only two cyano groups for each apical TCNE are coordinated to a neighboring V as opposed to fourfold coordination for equatorial TCNE. Additionally, the DFT calculations predict an optical bandgap of 0.8 eV, providing theoretical support for our experimentally measured bandgap of ~0.6 ± 0.18 eV. These results are, to the best of our knowledge, the first quantitative comparison of DFT calculations and experimental measurements of the electronic structure of $V[TCNE]_x$.

In addition to providing a measurement of the optoelectronic properties of a material, STEM EELS can also be used to probe the structural information. As stated in the Introduction, the general structure of $V[TCNE]_x$ is believed to be a 3D network of V^{2+} in octahedral coordination with six surrounding TCNE molecules, and the above calculations were performed using a $V[TCNE]_x$ crystal with the same parameters [Fig. 2(c)]. The high-loss EELS data collected from 260 to 570 eV contain the C K-edge, N K-edge, V $L_{2,3}$ edge, and the O K-edge if present [Fig. 3(a)]. The absence of the O K-edge indicates that the material was not oxidized during the sample transfer to the microscope. The V oxidation state of the V can be determined by the L_3 maximum position along the x axis of the EELS spectrum. According to the x-ray absorption near edge fine structure (XANES) data by Kortright *et al.*,[32] the L_3 peak for V^{2+} occurs at ~517 eV. Fitting a Gaussian peak to the L_3 edge in the deconvolved spectrum in Fig. 3(b) indicates that the center of this peak lies at 516.8 eV, confirming that the oxidation state of the CVD films is V^{2+}. While the V oxidation state has been measured previously, the methods used were spatially averaging techniques and it was unknown whether the V oxidation state varied within the $V[TCNE]_x$ film. Exploiting the high spatial resolution of STEM EELS spectrum imaging, spatial variations in the V oxidation state can be probed. Using a cross section of the thin film prepared using FIB (see Sec. II), it was demonstrated that there is no shift in the V L_3-peak maximum through the foil thickness, indicating that the oxidation state is homogeneous throughout $V[TCNE]_x$ films (Fig. S3).

EELS can also be used to provide insights on the local bonding environment by analysis of the energy-loss near edge fine structure (ELNES). For V^{2+} in a perfect octahedral environment, the L_2 peak (and to a lesser extent L_3) exhibits a complex multiplet structure arising from the interactions of crystal field splitting of the d orbitals, spin-orbit effects, and core hole effects that have been observed in previous XANES measurements of $V[TCNE]_x$.[32] Simulations of the ELNES using crystal field multiplet calculations confirm that V^{2+} in an octahedral environment exhibits a distinct "doublet" structure on the L_2 peak (Fig. S4). The experimental data [Fig. 3(b)] show the presence of this doublet structure on the L_2 peak and asymmetry of the L_3-peak. This is consistent with simulation and indicates that V in our CVD grown films is in a perfect octahedral environment. The difference in relative intensities of the doublet features in the L_2-peak has been attributed to back-bonding effects that are not included in the multiplet calculation.[32]

The C and N K-edges are not influenced by multiplet effects, and the sharp, intense peaks on both edges [Fig. 3(a)] arise from 1s-π^* transitions between well-defined atomic/molecular orbitals in the TCNE molecule.[32] Figure 3(c) shows non-linear least squares (NLLS) fitting of the C K-edge with four Gaussian peaks, making up the total 1s-π^* peak. The first two Gaussians at 284 and 285 eV are associated with C1s → $\pi^*_{C=C}$ transitions, while the higher energy Gaussian peaks at 286.5 and 287.8 eV are associated with

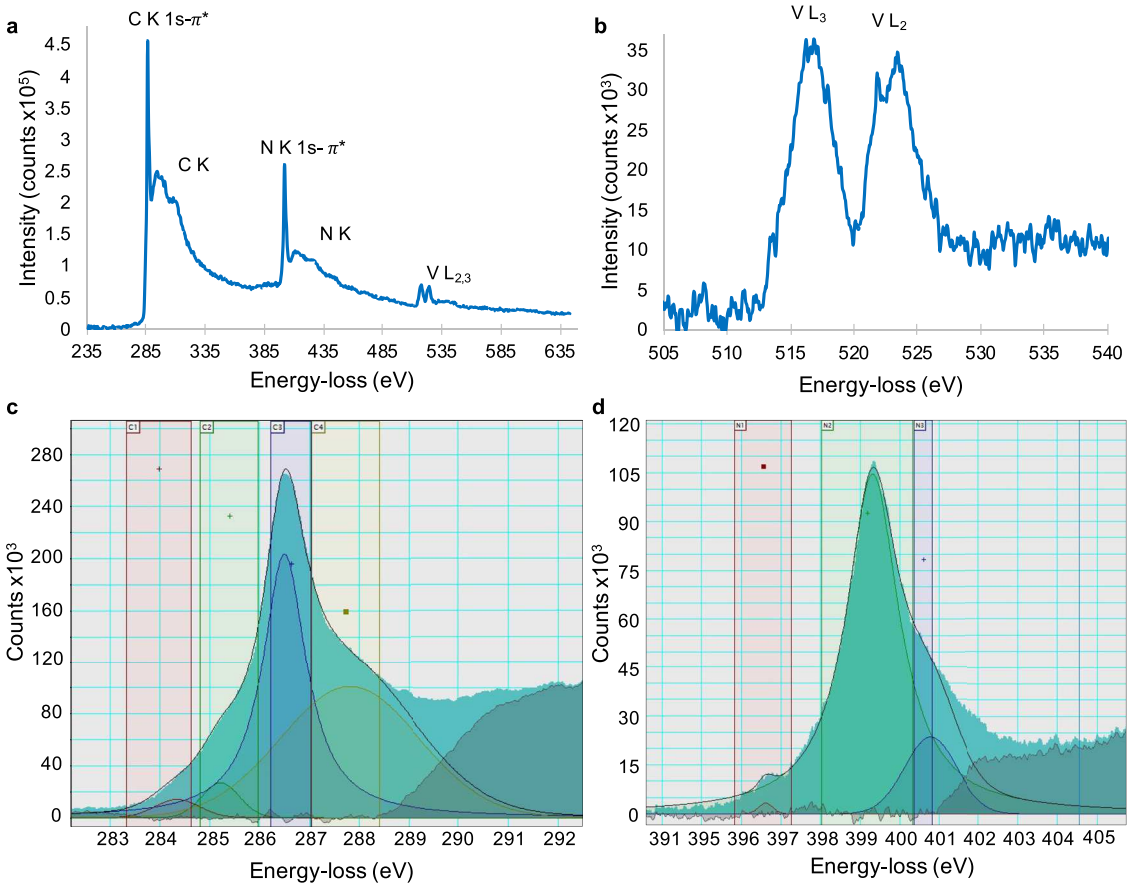

FIG. 3. (a) High-loss EELS data of plan-view V[TCNE]$_x$ showing the C K, N K, and V $L_{2,3}$ ionization edges. (b) Deconvolved EELS spectra of the V $L_{2,3}$ ionization edge with splitting observed on the L_2 peak, indicating that V is in a perfect octahedral environment. NLLS fitting of Gaussian peaks to the (c) C K-edge π^* and (d) N K-edge π^* peaks. The C K-edge shows four features associated with both C = C and C ≡ N, while the N K-edge shows three features associated with C ≡ N.

C1s → $\pi^*_{C\equiv N}$. The ~1 eV split between the π^* molecular orbitals (MOs) associated with both the C ≡ N and C = C bonds suggests that not all TCNE molecules are identical. This is consistent with the previously described DFT calculations that indicate the MOs associated with the apical ligands are shifted to higher energy relative to those on the equatorial ligands. Figure 3(d) shows the NLLS fitting of the N K-edge with three Gaussians at 396, 399, and 401 eV, which are all associated with N1s → $\pi^*_{C\equiv N}$ transitions. Multiple peaks arise for N due to the *p*–*d* mixing with V *d* orbitals. Additionally, one peak is likely associated with the small fraction of N atoms on the apical TCNE molecules that are not bonded to V^{2+}.

We have also established that the V L_2 doublet structure evolves as a function of both sample aging and oxidation. Thin films are deposited on multiple TEM grids during a CVD growth, which means samples grown under identical conditions can be compared. In Fig. 4(a), spectra from three plan-view samples grown under identical conditions are compared: (1) fresh (examined within a few hours of growth), (2) aged (stored for 1 week at room temperature in an argon glovebox (O_2, H_2O < 1.0 ppm), and (3) oxidized (exposed to air for >3 weeks). The V $L_{2,3}$ peaks of the fresh sample show asymmetry on the L_3 peak and a clear doublet splitting on the L_2 peak. In the aged sample, the fine structure is still present although less pronounced than the fresh specimen. Crucially, there is no evidence of an oxygen K-edge in either dataset. This indicates that the reduction of the splitting is due to aging rather than oxidation. As discussed earlier, V is in a perfect octahedral environment in the fresh sample, but it appears that over time, structural relaxation in the V[TCNE]$_x$ film occurs, which lowers the point symmetry at the V site, changing the local electronic structure, and, thus, suppresses the multiplet fine structure. This relaxation of the structural order in V[TCNE]$_x$ films is also reflected in Raman studies of V[TCNE]$_x$ films comparing fresh vs aged samples.[54] Raman spectroscopy of V[TCNE]$_x$ films directly validates the distortion about V as the V–N stretching mode features vanish upon aging, which is attributed to a change in the bonding between V and TCNE molecules.[54] We also note that the V L_2 peak from the cross-sectional FIB foils does not show a well-defined split in most cases, but rather matches that of the aged plan-view films, showing a hint of asymmetry. The C and N K-edges of the cross-sectional foils also lack the fine structure we see in the plan-view data, suggesting that the FIB process damages

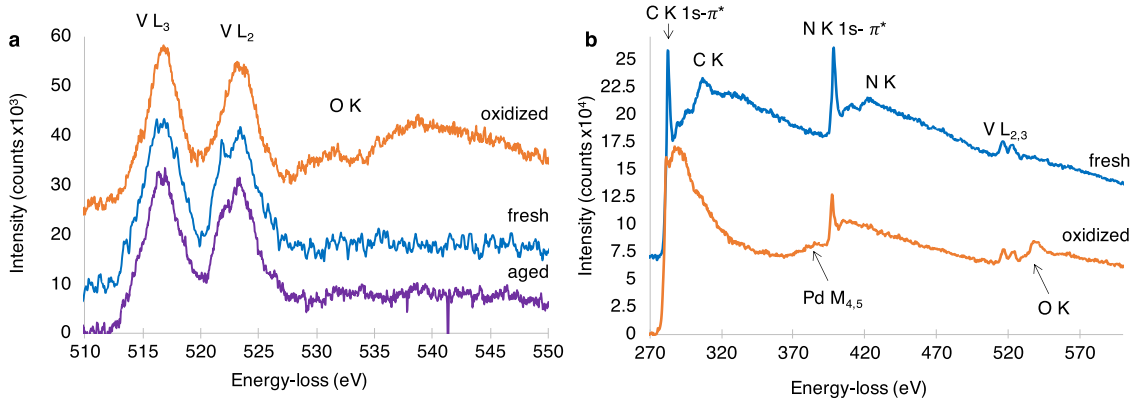

FIG. 4. (a) Deconvolved high-loss EELS data comparison of the V $L_{2,3}$ ionization edge for a fresh sample (blue), an oxidized sample (orange), and an aged sample (purple). The reduction of splitting on the L_2 peak indicates that the V octahedral environment becomes distorted in both oxidized and aged samples. (b) Low-dispersion high-loss data comparison of a fresh sample (blue) and an oxidized sample (orange), showing a reduction of C K 1s-π^* in the oxidized sample, suggesting that C = C is targeted during oxidation.

the films to some extent. Furthermore, the cross-sectional samples all have an Al capping layer to reduce the speed of oxidation. This Al capping layer was deposited using thermal evaporation, which could also contribute to thermal degradation of the cross-sectional samples, as indicated in Fig. S3b, in which we see more asymmetry on the L_2 peak in regions further from the Al capping layer.

In the oxidized sample [Fig. 4(a)], spectral intensity in the 530–550 eV range is attributed to the oxygen K-edge excitation and is consistent with oxidized specimens previously analyzed using XAFS.[32] In addition to the presence of the O K-edge, the L_2 doublet structure has completely disappeared, indicating that the local point symmetry at the V site is further reduced. However, there is no change in energy-loss of the V edge, indicating that the V oxidation state remains as V^{2+}. This intriguing observation is consistent with changes observed at the C K-edge upon oxidation. Figure 4(b) shows EELS data of the fresh and oxidized specimens. It is apparent that the peak associated with 1s-π^* transitions at the C K-edge is significantly reduced on oxidation. In contrast, the 1s-π^* peak at the N K-edge remains sharp and intense. The broad peak before the N K-edge is the Pd $M_{4,5}$ edge from the Pd Substratek TEM grids. There is no Pd peak in the fresh spectrum as that specimen was grown on a Pt Substratek TEM grid; however, both samples are from the same growth as described in the methodology section. These observations give clear mechanistic insights into the oxidation process, indicating that oxygen attacks the C = C double bond in the TCNE molecules. This will result in transforming C from sp^2 to sp^3 coordination, and thus, the TCNE molecule is no longer planar. The sp^3 environment allows for (relatively) free rotation around the new C–C single bond, which will distort the local point symmetry at the V site, therefore reducing or eliminating the observed fine structure on the V L_2 peak. These TEM results may also provide additional insights into the progression of the C = C stretching mode peaks seen in the Raman spectra of aged films, which see a significant broadening and a change in the relative intensity between the two dominant peaks.[54] How these features change with age may reflect not only the structural relaxation in the material but perhaps also the oxidation, targeting C = C naturally occurring in encapsulated films as they age in atmospheric conditions. With these new insights into the oxidation mechanism of $V[TCNE]_x$ films and the success of this DFT model, the origin of these spectral changes may be revealed and identified both experimentally and theoretically.

IV. CONCLUSIONS

We used electron microscopy and density functional theory methods to study and reveal previously unknown properties of the quantum information relevant material, $V[TCNE]_x$. Low-loss EELS measurements align quantitatively with DFT calculations, concretely establishing the optoelectronic properties of $V[TCNE]_x$. We measure a bandgap of 0.6 eV, which is close to the 0.8 eV optical gap of the DFT band structure calculations and ~0.5 eV bandgap from past transport methods. Our DFT calculations identify multiple single electron transitions observed in the low-loss EELS data, including features from Hubbard U on the *p* and *d* states and the apical/equatorial ligand field splittings. Through analysis of high-loss EELS data, we have shown that our CVD grown films of $V[TCNE]_x$ contain V in an oxidation state 2+, which does not change spatially. Splitting on the V L_2 peak is observed, indicating that V is in a perfect octahedral environment. EELS measurements on oxidized and aged films show that this V splitting decreases upon aging and oxidation independently of each other, therefore establishing two distinct degradation mechanisms of $V[TCNE]_x$. The reduction of the C K-edge 1s-π^* peak suggests that the carbon–carbon double bond of the TCNE molecules is targeted during oxidation. This change from sp^2 to sp^3 forces the carbon to a tetrahedral geometry, therefore distorting the octahedral environment of the V and eliminating the doublet structure on the V L_2 peak. These findings help elucidate the structure of $V[TCNE]_x$ and establish the theoretical framework necessary to predict and study the family of related metal–ligand magnetic materials.[55–60]

SUPPLEMENTARY MATERIAL

See the supplementary material for EELS data collected from a FIB foil, the partial density of states for majority and minority spins, and the simulated $L_{2,3}$ V edge.

ACKNOWLEDGMENTS

The authors would like to thank Dr. Jessica Alexander for her contributions to the FIB and EELS procedures used in this work. V[TCNE]$_x$ synthesis (S.W.K., M.C., and E.J.-H.) was supported by the NSF under Grant No. DMR 1808704. The electron microscopy experiments (A.H.T. and D.W.M.) were supported by the Center of Emergent Materials, an NSF MRSEC, under Award Nos. DMR-2011876 and DMR-1420451. Theoretical calculations (M.E.F. and Y.S.) were supported by the NSF under Grant No. DMR-1808742.

AUTHOR DECLARATIONS

Conflict of Interest

The authors have no conflicts to disclose.

Author Contributions

Amanda H. Trout: Data curation (lead); Formal analysis; Investigation; Methodology; Validation (equal); Writing – original draft (lead); Writing – review & editing (equal). **Seth W. Kurfman:** Data curation (supporting); Formal analysis; Investigation; Methodology; Writing – review & editing (equal). **Yueguang Shi:** Data curation (supporting); Formal analysis (supporting); Investigation (supporting); Methodology (supporting); Writing – original draft (supporting); Writing – review & editing (supporting). **Michael Chilcote:** Writing – review & editing (supporting). **Michael E. Flatté:** Conceptualization (equal); Funding acquisition (equal); Validation (equal); Writing – original draft (supporting); Writing – review & editing (equal). **Ezekiel Johnston-Halperin:** Conceptualization (equal); Funding acquisition (equal); Project administration (equal); Supervision (equal); Validation (equal); Writing – original draft (supporting); Writing – review & editing (equal). **David W. McComb:** Conceptualization (equal); Funding acquisition; Project administration; Supervision; Validation; Writing – original draft (supporting); Writing – review & editing (equal).

DATA AVAILABILITY

The data that support the findings of this study are available from the corresponding author upon reasonable request.

REFERENCES

[1] D. J. Reilly, "Engineering the quantum-classical interface of solid-state qubits," npj Quantum Inf. **1**, 15011 (2015).
[2] D. Lachance-Quirion *et al.*, "Entanglement-based single-shot detection of a single magnon with a superconducting qubit," Science **367**, 425 (2020).
[3] D. Lachance-Quirion, Y. Tabuchi, A. Gloppe, K. Usami, and Y. Nakamura, "Hybrid quantum systems based on magnonics," Appl. Phys. Express **12**, 070101 (2019).
[4] D. R. Candido, G. D. Fuchs, E. Johnston-Halperin, and M. E. Flatté, "Predicted strong coupling of solid-state spins via a single magnon mode," Mater. Quantum Technol. **1**, 011001 (2021).
[5] A. A. Serga, A. V. Chumak, and B. Hillebrands, "YIG magnonics," J. Phys. D: Appl. Phys. **43**, 264002 (2010).
[6] P. Pirro, V. I. Vasyuchka, A. A. Serga, and B. Hillebrands, "Advances in coherent magnonics," Nat. Rev. Mater. **6**, 1114 (2021).
[7] K.-i. Uchida *et al.*, "Observation of longitudinal spin-Seebeck effect in magnetic insulators," Appl. Phys. Lett. **97**, 172505 (2010).
[8] A. A. Clerk, K. W. Lehnert, P. Bertet, J. R. Petta, and Y. Nakamura, "Hybrid quantum systems with circuit quantum electrodynamics," Nat. Phys. **16**, 257 (2020).
[9] C. Hauser *et al.*, "Yttrium iron garnet thin films with very low damping obtained by recrystallization of amorphous material," Sci. Rep. **6**, 20827 (2016).
[10] N. Zhu *et al.*, "Organic ferrimagnetic material vanadium tetracyanoethylene for non-reciprocal microwave applications," in *2020 IEEE/MTT-S International Microwave Symposium (IMS)* (IEEE, 2020), p. 528.
[11] A. Franson *et al.*, "Low-damping ferromagnetic resonance in electron-beam patterned, high-Q vanadium tetracyanoethylene magnon cavities," Appl. Phys. Lett. Mater. **7**, 121113 (2019).
[12] H. Yusuf *et al.*, "Exploring a quantum-information-relevant magnonic material: Ultralow damping at low temperature in the organic ferrimagnet V[TCNE]$_x$," AVS Quantum Sci. **3**, 026801 (2021).
[13] M. Chilcote *et al.*, "Spin-wave confinement and coupling in organic-based magnetic nanostructures," APL Mater. **7**, 111108 (2019).
[14] N. Zhu *et al.*, "Low loss spin wave resonances in organic-based ferrimagnet vanadium tetracyanoethylene thin films," Appl. Phys. Lett. **109**, 082402 (2016).
[15] C.-J. Yu, S. von Kugelgen, D. W. Laorenza, and D. E. Freedman, "A molecular approach to quantum sensing," ACS Cent. Sci. **7**, 712 (2021).
[16] S. L. Bayliss *et al.*, "Optically addressable molecular spins for quantum information processing," Science **370**, 1309 (2020).
[17] M. R. Wasielewski *et al.*, "Exploiting chemistry and molecular systems for quantum information science," Nat. Rev. Chem. **4**, 490 (2020).
[18] K. I. Pokhodnya, A. J. Epstein, and J. S. Miller, "Thin-film V[TCNE]$_x$ magnets," Adv. Mater. **12**, 410 (2000).
[19] G. C. De Fusco, L. Pasani, B. Montanari, and N. M. Harrison, "Density functional study of the magnetic coupling in V(TCNE)$_2$," Phys. Rev. B **79**, 085201 (2009).
[20] M. Harberts, Y. Lu, H. Yu, A. J. Epstein, and E. Johnston-Halperin, "Chemical vapor deposition of an organic magnet, vanadium tetracyanoethylene," J. Vis. Exp. **101**, e52891 (2015).
[21] I. H. Froning *et al.*, "Thin-film encapsulation of the air-sensitive organic-based ferrimagnet vanadium tetracyanoethylene," Appl. Phys. Lett. **106**, 122403 (2015).
[22] H. Yu *et al.*, "Ultra-narrow ferromagnetic resonance in organic-based thin films grown via low temperature chemical vapor deposition," Appl. Phys. Lett. **105**, 012407 (2014).
[23] H. Casellas, D. de Caro, L. Valade, and P. Cassoux, "A new chromium-based molecular magnet grown as a thin film by CVD," Chem. Vap. Deposition **8**, 145 (2002).
[24] E. Lamouroux, D. de Caro, and L. Valade, "Molybdenum-tetracyanoethylene-based thin film magnets prepared by chemical vapor deposition: Effect of deposition temperature on morphology," Thin Solid Films **467**, 93 (2004).
[25] Y. A. Getmanenko *et al.*, "Magnetic ordering in a vanadium-organic coordination polymer using a pyrrolo[2,3-*d*:5,4-*d*′] bis(thiazole)-based ligand," RCS Adv. **8**, 36223 (2018).
[26] D. S. Tatum, J. M. Zadrozny, and G. T. Yee, "A new family of high T_c molecule-based magnetic networks: V[*x*-Cl$_n$PTCE]$_2$·yCH_2Cl_2 (PTCE = phenyltricyanoethylene)," Magnetochemistry **5**, 44 (2019).
[27] Y. Lu *et al.*, "Thin-film deposition of an organic magnet based on vanadium methyl tricyanoethylenecarboxylate," Adv. Mater. **26**, 7632 (2014).
[28] Y. Lu, H. Yu, M. Harberts, A. J. Epstein, and E. Johnston-Halperin, "Vanadium[ethyl tricyanoethylene carboxylate]$_x$: A new organic-based magnet," J. Mater. Chem. C **3**, 7363 (2015).
[29] H. Matsuura, K. Miyake, and H. Fukuyama, "Theory of room temperature ferromagnet V(TCNE)$_x$ ($1.5 < x < 2$): Role of hidden flat bands," J. Phys. Soc. Jpn. **79**, 034712 (2010).

[30]J. S. Miller, "Oliver Kahn Lecture: Composition and structure of the V[TCNE]$_x$ (TCNE = tetracyanoethylene) room-temperature, organic-based magnet—A personal perspective," Polyhedron **28**, 1596 (2009).
[31]C. Tengstedt, M. P. de Jong, A. Kanciurzewska, E. Carlegrim, and M. Fahlman, "X-ray magnetic circular dichroism and resonant photomission of V(TCNE)$_x$ hybrid magnets," Phys. Rev. Lett. **96**, 057209 (2006).
[32]J. B. Kortright, D. M. Lincoln, R. Shima Edelstein, and A. J. Epstein, "Bonding, backbonding, and spin-polarized molecular orbitals: Basis for magnetism and semiconducting transport in V[TCNE]$_{x\sim2}$," Phys. Rev. Lett. **100**, 257204 (2008).
[33]D. Haskel *et al.*, "Local structural order in the disordered vanadium tetracyanoethylene room-temperature molecular-based magnet," Phys. Rev. B **70**, 054422 (2004).
[34]D. Haskel *et al.*, Local structure of amorphous V[TCNE]$_x$ molecular magnet, https://www.aps.anl.gov/sites/.
[35]G. Kresse and J. Hafner, "Norm-conserving and ultrasoft pseudopotentials for first-row and transition elements," J. Condens. Matter Phys. **6**, 8245 (1994).
[36]G. Kresse and D. Joubert, "From ultrasoft pseudopotentials to the projector augmented-wave method," Phys. Rev. B **59**, 1758 (1999).
[37]H. Suhl, "Ferromagnetic resonance in nickel ferrite between one and two kilomegacycles," Phys. Rev. **97**, 555 (1955).
[38]J. Smit and H. G. Beljers, "Ferromagnetic resonance absorption in $BaFe_{12}O_{19}$: A highly anisotropic crystal," Philips Res. Rep. **10**, 113 (1955).
[39]B. A. McCullian *et al.*, "Broadband optical detection of ferromagnetic resonance from the organic-based ferrimagnet V[TCNE]$_x$ using N-V centers in diamond," Phys. Rev. Appl. **14**, 024033 (2020).
[40]V. N. Prigodin, N. P. Raju, K. I. Pokhodnya, J. S. Miller, and A. J. Epstein, "Spin-driven resistance in organic-based magnetic semiconductor V[TCNE]$_x$," Adv. Mater. **14**, 1230 (2002).
[41]V. N. Prigodin, N. P. Raju, K. I. Pokhodnya, J. S. Miller, and A. J. Epstein, "Electron spin-driven resistance in organic-based magnetic semiconductor V[TCNE]$_x$," Synth. Met. **135-136**, 87 (2003).
[42]K. Pokhodnya, M. Bonner, V. Prigodin, A. J. Epstein, and J. S. Miller, "Carrier transport in the V[TCNE]$_x$ (TCNE = tetracyanoethylene; $x \sim 2$) organic-based magnet," J. Condens. Matter Phys. **25**, 196001 (2013).
[43]N. P. Raju, V. N. Prigodin, K. I. Pokhodnya, J. S. Miller, and A. J. Epstein, "High field linear magnetoresistance in fully spin-polarized high-temperature organic-based ferrimagnetic semiconductor V(TCNE)$_x$ film, $x \sim 2$," Synth. Met. **160**, 307 (2010).
[44]R. F. Egerton, *Electron Energy-Loss Spectroscopy in the Electron Microscope* (Springer, 2011).
[45]DigitalMicrograph 3.4 User's GuideGatan, Inc., 1999.
[46]M. Fox, *Optical Properties of Solids* (Oxford University Press, 2001).
[47]J. A. Alexander, *High-Resolution Electron Energy-Loss Spectroscopy of Beam-Sensitive Functional Materials* (The Ohio State University, 2018).
[48]G. Kresse and J. Hafner, "*Ab initio* molecular dynamics for liquid metals," Phys. Rev. B **47**, 558 (1993).
[49]G. Kresse and J. Hafner, "*Ab initio* molecular-dynamics simulation of the liquid-metal–amorphous-semiconductor transition in germanium," Phys. Rev. B **49**, 14251 (1994).
[50]G. Kresse and J. Furthmüller, "Efficiency of *ab initio* total energy calculations for metals and semiconductors using a plane-wave basis set," Comput. Mater. Sci. **6**, 15 (1996).
[51]G. Kresse and J. Furthmüller, "Efficient iterative schemes for *ab initio* total-energy calculations using a plane-wave basis set," Phys. Rev. B **54**, 11169 (1996).
[52]J. P. Perdew, K. Burke, and M. Ernzerhof, "Generalized gradient approximation made simple," Phys. Rev. Lett. **78**, 1396 (1996).
[53]J. Heyd, G. E. Scuseria, and M. Ernzerhof, "Hybrid functionals based on a screened Coulomb potential," J. Chem. Phys. **118**, 8207 (2003).
[54]H. F. H. Cheung *et al.*, "Raman spectroscopy of aging of the low-loss ferrimagnet vanadium tetracyanoethylene," J. Phys. Chem. C **125**, 20380 (2021).
[55]P. Perlepe *et al.*, "Metal-organic magnets with large coercivity and ordering temperatures up to 242 °C," Science **370**, 587 (2020).
[56]M. G. F. Vaz and M. Andruh, "Molecule-based magnetic materials constructed from paramagnetic organic ligands and two different metal ions," Coord. Chem. Rev. **427**, 213611 (2021).
[57]J.-H. Wang, Z.-Y. Li, M. Yamashita, and X.-H. Bu, "Recent progress in cyano-bridged transition-metal-based single-molecule magnets and single-chain magnets," Coord. Chem. Rev. **428**, 213617 (2021).
[58]D. R. Talham and M. W. Meisel, "Thin films of coordination polymer magnets," Chem. Soc. Rev. **40**, 3356 (2011).
[59]J. Ferrando-Soria *et al.*, "Molecular magnetism, *quo vadis*? A historical perspective from a coordination chemist viewpoint," Coord. Chem. Rev. **339**, 17–103 (2021).
[60]M. D. Harvey, T. D. Crawford, and G. T. Yee, "Room-temperature and near-room-temperature molecule-based magnets," Inorg. Chem. **47**, 5649–5655 (2008).